Deriving grain boundary character distributions and relative grain boundary energies from three-dimensional EBSD data

G. S. Rohrer*[1], J. Li[1], S. Lee[1], A. D. Rollett[1], M. Groeber[2] and M. D. Uchic[2]

Three-dimensional electron backscatter diffraction data, obtained by serial sectioning a nickel–base superalloy, has been analysed to measure the geometric arrangement of grain boundary planes at triple junctions. This information has been used to calculate the grain boundary character distribution (GBCD) and the grain boundary energy distribution (GBED). The twin content from the three-dimensional GBCD calculation compares favourably with the twin content estimated by stereology. Important factors in the analysis are the alignment of the parallel layers, the ratio of the out-of-plane to in-plane spacing of the discrete orientation data and the discretisation of the domain of grain boundary types. The results show that grain boundaries comprised of (111) planes occur most frequently and that these grain boundaries have a relatively low energy. The GBCD and GBED are inversely correlated.

This paper is part of a special issue on 'Applications of electron backscatter diffraction'

Introduction

Microstructures have traditionally been characterised on the basis of observations of two-dimensional plane sections. Recognising that microstructures are actually comprised of three-dimensional objects, stereological techniques have been developed to extract three-dimensional information from two-dimensional observations. However, such information is always constrained by certain assumptions about the distribution, shape and orientations of the microstructural components. Furthermore, stereological analysis produces statistical information about groups of objects instead of quantities that can be associated with specific objects.

The focus of the current paper is on determining the orientations of grain boundary planes and the geometries of triple lines within polycrystalline structures. In the past, serial sectioning by polishing or milling, combined with electron backscatter diffraction (EBSD) mapping, has been used to determine grain boundary plane orientations.[1–5] However, the limited use of this technique over the years is evidence of the method's difficulty. Stereology, on the other hand, has been applied extensively.[6–13] However, this provides information about the distributions of planes, not specific planes or the configuration of the planes at triple lines.

The development of the dual beam focused ion beam SEM makes it possible to automate the serial sectioning and EBSD mapping processes. The experiment consists of removing a thin layer of material via cross-section ion milling, followed by the collection of an EBSD map, and this cycle is repeated until the desired volume of material has been characterised. The possibility of performing tomographic EBSD mapping and subsequent reconstruction of grain microstructures in three dimensions has already been demonstrated.[14–19] The results show that it is possible to measure several characteristics of the grain level microstructure, including the distribution of grain sizes, shapes and orientations.

Methods have also been developed to compute the grain boundary character distribution (GBCD) and, from the geometries of the triple lines, the relative grain boundary energy distribution (GBED) from three-dimensional EBSD data.[20,21] The purposes of the current paper are to describe in detail the processes used to evaluate the GBCD and to demonstrate the efficacy of the procedures. The procedures are applied to data from a Ni base superalloy with a high degree of twining; the twins act as an internal standard against which the authors' results can be compared. Using the twins as a guide, the authors find that appropriate discretisation and layer to layer alignment are the most important factors in determining accurate interface geometry. The resulting GBCD and GBED are presented as a demonstration of the method.

Methods

The procedures for data collection have already been described in detail.[14,15,18,19] Here, new information (the GBCD and GBED) is derived from these same data. The sample is a powder processed Ni base superalloy (IN100)

[1]Department of Materials Science and Engineering, Carnegie Mellon University, Pittsburgh, PA 15213, USA
[2]Air Force Research Laboratory, Materials and Manufacturing Directorate, AFRL/MLLMD, Wright-Patterson AFB, Dayton, OH 45433, USA

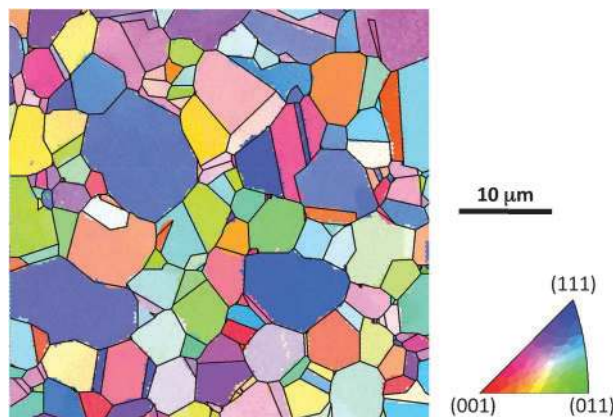*Corresponding author, email gr20@andrew.cmu.edu
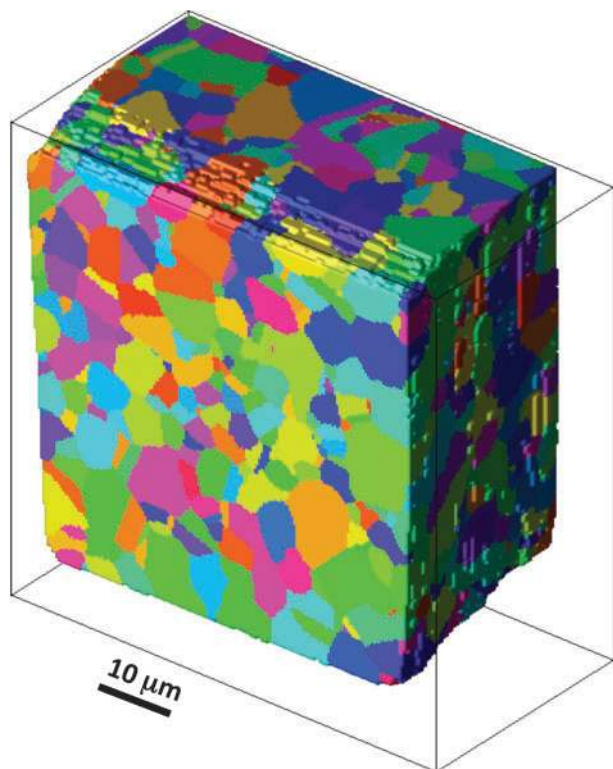
1 **Three-dimensional rendering of 96 aligned layers of orientation data for Ni base superalloy: grains are assigned random colours**

2 **Inverse pole figure map of one layer of data: grains are coloured according to the orientations given in legend; reconstructed grain boundary line segments (black lines) are superimposed on map**

with a mean grain diameter of ~ 3 μm. The microstructure of this nickel superalloy consists of a γ matrix that contains large volume fraction of γ' precipitates. However, the phases were not resolved by the EBSD study, so each grain is considered to be single phase.

The data consists of 170 parallel EBSD maps. Each map has a lateral resolution of 0·25 μm, has a 45×45 μm field of view and is separated in the out-of-plane direction by 0·25 μm. The analysis steps the authors use can be divided into two groups: those that can be carried out using commercially available three-dimensional OIM visualisation software (EDAX, Mahwah, NJ, USA) and those for which the authors use software developed at Carnegie Mellon. For example, in the initial steps using the commercial OIM software, the data were cropped to remove unindexed points at the periphery of each image. The EBSD data were cleaned using two iterations of grain dilation in the OIM software with a minimum grain size of 10 pixels. This procedure considers any grouping of less than 10 pixels, with disorientations of less than 5°, to be insufficient to define a single grain and assigns their orientation to match the orientation of an adjacent grain. A single average orientation was assigned to each grain, with an individual grain being defined as a set of pixels whose disorientations lie within 5° of one another.

The next step is to align the layers so that they are spatially registered to a common reference frame. This is necessary because of misalignments introduced by the need to reposition and rotate the sample between each milling and EBSD mapping step. At this stage, the data were aligned on a fixed grid. This will be referred to as primary alignment. The three-dimensional OIM visualisation software can perform the primary alignment by maximising the cross-correlation between the three different colour channels in the orientation image map. A procedure that minimises the disorientation between corresponding voxels on adjacent layers was also developed, and an image of a portion of the data aligned in this way is shown in Fig. 1.[22] Both methods preserve a fixed grid for the data and produce comparable results; the latter method was used for the results presented here.

The next step is to approximate the grain boundaries on each layer with straight line segments. Again, this can be accomplished with the commercial OIM software as long as the data are on a hexagonal grid. The data analysed here were acquired on a square grid, so it was converted to a hexagonal grid using the freely available program, OIMTools.[23] With the orientations on a hexagonal grid, the OIM software was used to determine grain boundary line segments approximating the true positions for the boundaries according to a procedure described in Ref. 24. For the line segment extraction, a maximum deviation of 2 pixels was permitted between the actual boundary position and the reconstructed line segment. An example of the reconstructed grain boundary line segments, superimposed on the EBSD map, is shown in Fig. 2. The segmentation makes the boundaries appear polygonal. However, it should be noted that the segmented approximation for the boundary network is constrained to lie within 2 pixels of the true boundary at all positions. For each layer, the OIM software produces a list of line segments that specifies, among other things, the Euler angles for the grains on either side of the line and the initial and final coordinates. The remainder of the analysis is carried out on these lists of line segments using software developed at Carnegie Mellon.

The first step of calculating the GBCD and GBED is to locate each triple junction. On each layer, the list of line segments is searched to identify all groups of three line segments whose end points share an identical coordinate. These triplets are then saved. After all of the triple junctions are identified on each layer, they are compared. To find triple junctions on adjacent layers that are connected by a triple line, the lateral coordinates of each triple junction are compared. For the five junctions on an adjacent layer that have the closest
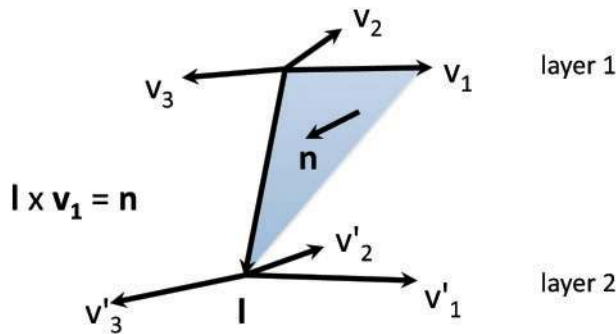
3 Schematic illustrating calculation of grain boundary normals: three grain boundary line segments on layer one v_i meet at triple junction; three related segments v'_i meet on adjacent layer 2; triple line vector *l* joins junctions from layer 1 to 2; by crossing it with each line segment, a grain boundary normal *n* is generated

lateral coordinates, the three crystal orientations on the first layer are compared to the three on the second layer. If the disorientations between the crystals on the top and bottom layers are all less than $5°$, a triple line is assumed to connect the two triple junctions between the layers. Because some topological changes occur between the section planes, only a fraction of all of the triple junctions can be matched. Typically, 70–90% of the junctions on each layer are matched to a junction on an adjacent layer.

The triple junction is now characterised by three vectors on each layer and a vector connecting them along the triple line, as illustrated in Fig. 3. The data are sorted so that the vectors are listed in counterclockwise order around the line. The grain boundary normal orientation is now determined by the cross-product of *l* and v_i. The area of the boundary plane is one-half of the magnitude of the cross-product. The three vectors on the top layer produce three normal vectors, and the three on the lower layer produce three more. The area of each of these triangles is added to the appropriate discrete grain boundary type, determined by its misorientation and boundary normal. The five-dimensional space of grain boundary types is discretised as described earlier.[25] The normalised sums of these areas make up the GBCD.

In an equiaxed microstructure, one expects the orientations of the triple lines to be randomly distributed about the sample normal direction. However, when the triple line directions are examined, their distribution is typically biased. For example, Fig. 4 shows the directions of 118 triple lines between the second and third layers of the data. The circles represent the positions of the lines, and because they are on a discrete grid, many of the points overlap. The lines clearly are biased in the positive *y* direction. Assuming that this is due to an alignment error, a rigid shift can be applied to the coordinates of the third layer, so that the average triple line direction is perpendicular to the surface. This rigid shift is referred to as the secondary alignment procedure. The shifted data are represented by the red squares, and the shift is shown by the black arrow. The shifts applied to all 170 layers are shown in Fig. 5. The displacements in the vertical *y* direction are larger than the horizontal *x* component. This is probably because the sample is tilted by $70°$ with respect to the beam so that positioning errors in the *y* direction are magnified by a factor of
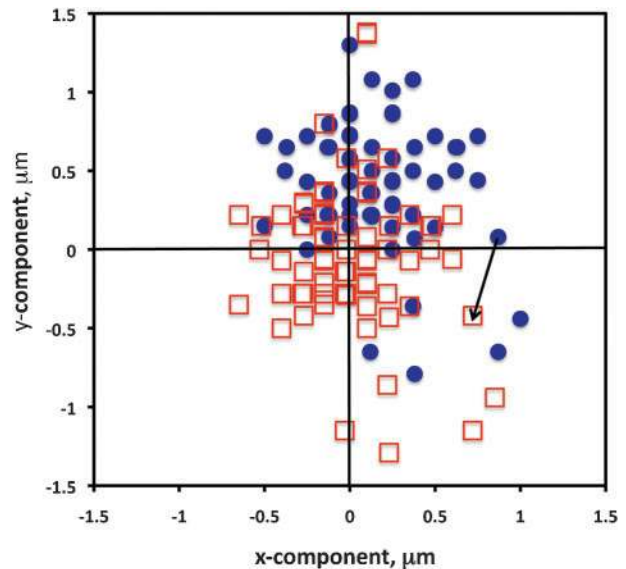

4 *x* and *y* components of 118 triple junctions between second and third layers (blue circles): red squares are same data, after aligning, so that average of all of components equals zero; black arrow connecting one of circles to square illustrates rigid shift applied to data

about 3 [1/cos (70)]. Note that the secondary alignment moves the data off of the fixed grid. To test the efficacy of this procedure, data with and without the secondary alignment will be compared in the results section.

Because the out-of-plane spacing is the same as the in-plane spacing, the triple lines are constrained to adopt discrete orientations in the sample reference frame, as depicted schematically in Fig. 6. To test the effect of this discretisation, the procedures described above were repeated, except that triple junctions were matched from every second layer. In other words, triple junctions on the first layer were matched with junctions on the third layer, and triple junctions on the second layer were matched with junctions on the fourth; these two patterns for resampling the data were extended throughout the
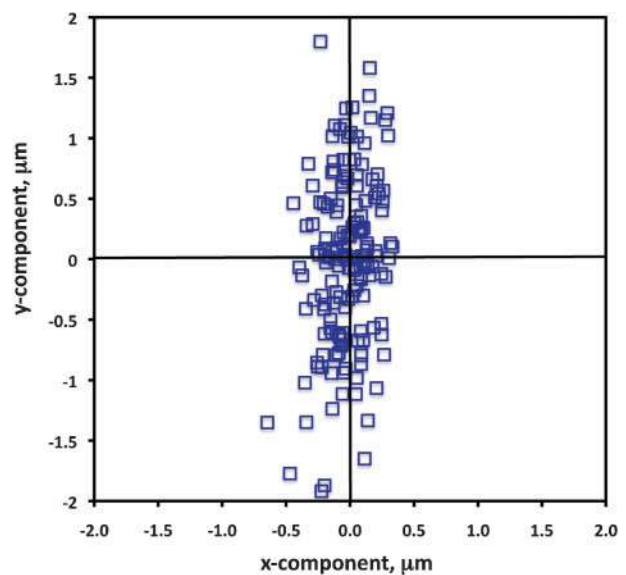
5 *x* and *y* components of shifts between all 170 layers: black arrow in Fig. 4 is represented as one point on this plot
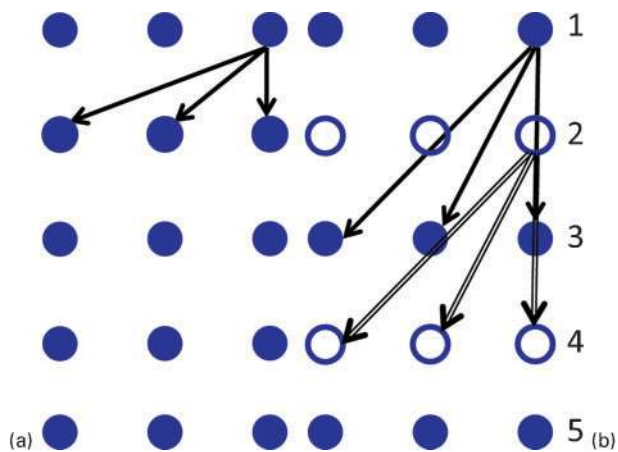
6 Schematic illustration of effect of out-of-plane to in-plane spacing ratio on triple line discretisation: Triple lines (arrows) must connect discrete voxels (circles) on adjacent layers; As out-of-plane spacing increases with respect to in-plane spacing, there are more possible inclinations for triple line; data were analysed using both *a* 1 : 1 spacing and, by resampling the same data set, *b* 2 : 1 spacing

dataset. Increasing the ratio of the out-of-plane to in-plane spacing from 1 : 1 to 2 : 1 decreases the minimum angular separation between two discrete triple line directions, as illustrated in Fig. 6.

The grain boundary energies were calculated using the capillarity vector method, developed by Morawiec.[26] The capillarity vector reconstruction method is similar to many other interface energy measurements in that the experimental observable is the interfacial geometry; the energy is computed from the geometry using an expression for interfacial equilibrium. In this case, the equilibrium at the triple line is described by the Herring[27] equation. Therefore, the key assumption underpinning this and previous measurements of relative grain boundary energies is that the interfacial junctions are in local thermodynamic equilibrium.

The capillary vector reconstruction method was described in detail in Ref. 26 and first applied to real data in Ref. 28. The current energy calculation was carried out in exactly the same way, using the same computer programs that were used in Refs. 26 and 28. Here, only a brief summary of the method is presented. The Herring[27] condition, when expressed in terms of capillarity vectors,[29,30] is

$$(\xi^1 + \xi^2 + \xi^3) \propto l = 0 \qquad (1)$$

where ξ^1, ξ^2 and ξ^3 are the capillarity vectors associated with the three grain boundaries and l is the triple line. Each capillarity vector has a component perpendicular to the grain boundary whose magnitude is equal to the relative grain boundary energy. Each capillarity vector also has a component tangent to the boundary whose magnitude is the differential of the energy with respect to a right handed rotation about l. The normal and tangent vectors for 15 000 grain boundary triple junctions have been measured (using an out-of-plane to in-plane spacing ratio of 2 : 1), and equation (1) can be applied to each junction. The unknowns, which are the magnitudes of the capillarity vectors, are determined by an iterative procedure that finds the set of ξ that most

nearly satisfy the 15 000 equilibrium equations. The final result was smoothed by replacing the value of ξ in each cell with the average of that vector and the vectors in the adjacent cells. The relative grain boundary energy is given by $\gamma = \xi \cdot n$, where n is the grain boundary normal. Previous calculations using simulated data based on model energy functions showed that the capillarity vector method reproduced all of the trends in the function, but did not quantitatively reproduce the depths of cusps.[26,28] Based on these findings, it is assumed that actual GBED is more anisotropic than the reconstructed distribution presented here.

Results

To test the efficacy of the reconstruction procedure, the GBCD at the Σ3 misorientation, which is a 60° rotation about the [111] axis can be examined. First, the authors compute the GBCD by an established stereological procedure.[6] The resulting distribution of grain boundary planes for the Σ3 misorientation is shown in Fig. 7*a*. The results are plotted in stereographic projection and are represented in multiples of random distribution (MRD) units. These units are computed by dividing the total area of a given grain boundary type by the average area per boundary type. The large peak of 1100 MRD at the (111) orientation corresponds to the pure twist configuration, which, in this case, is the coherent twin.

The distribution of grain boundary planes from the three-dimensional measurement, with a 1 : 1 ratio of the out-of-plane to in-plane spacing and without secondary alignment, is shown in Fig. 7*b*. The peak of the distribution for the twin (240 MRD) is less than that determined stereologically, and this suggests that the grain boundary plane orientations are not accurately determined. When the calculation is repeated with a 2 : 1 ratio of the out-of-plane to in-plane spacing, the twin population increases to 390 MRD. When the calculation is repeated after the secondary alignment procedure (but a 1 : 1 ratio of the out-of-plane to in-plane spacing), the twin population increases to 670 MRD. Finally, if the calculation is repeated using both the 2 : 1 ratio and the secondary alignment, the population increases to 1090 MRD, essentially identical to the stereologically determined population. The distribution of grain boundary planes for this calculation is shown in Fig. 7*c*.

It is possible to get a reliable estimate of the total fractional area of coherent twins within the microstructure by a second method.[24] For all boundary segments with the Σ3 misorientation (within Brandon's[31] criterion), the orientation of the segment can be compared to the orientation of the ideal twin plane. If the segment is within $\pm 10°$ of the ideal orientation, it is assumed to be a coherent twin. Analysing data in this way, the authors find that twin boundaries make up 21·9% of all of the grain boundary length observed on the plane sections. With a 10° discretisation, there are ~6500 discrete grain boundary types. Therefore, assuming that all of the twins are classified as a single type, the distribution at this point should have a value of 1400 MRD. The computed values of ~1100 MRD differ by more than 20% from this estimate.

One source of this deviation lies in an unfortunate choice of the discretisation of grain boundary types, which divides each angular range of 90° into nine discrete categories.[25] The ideal Euler angles for the twin
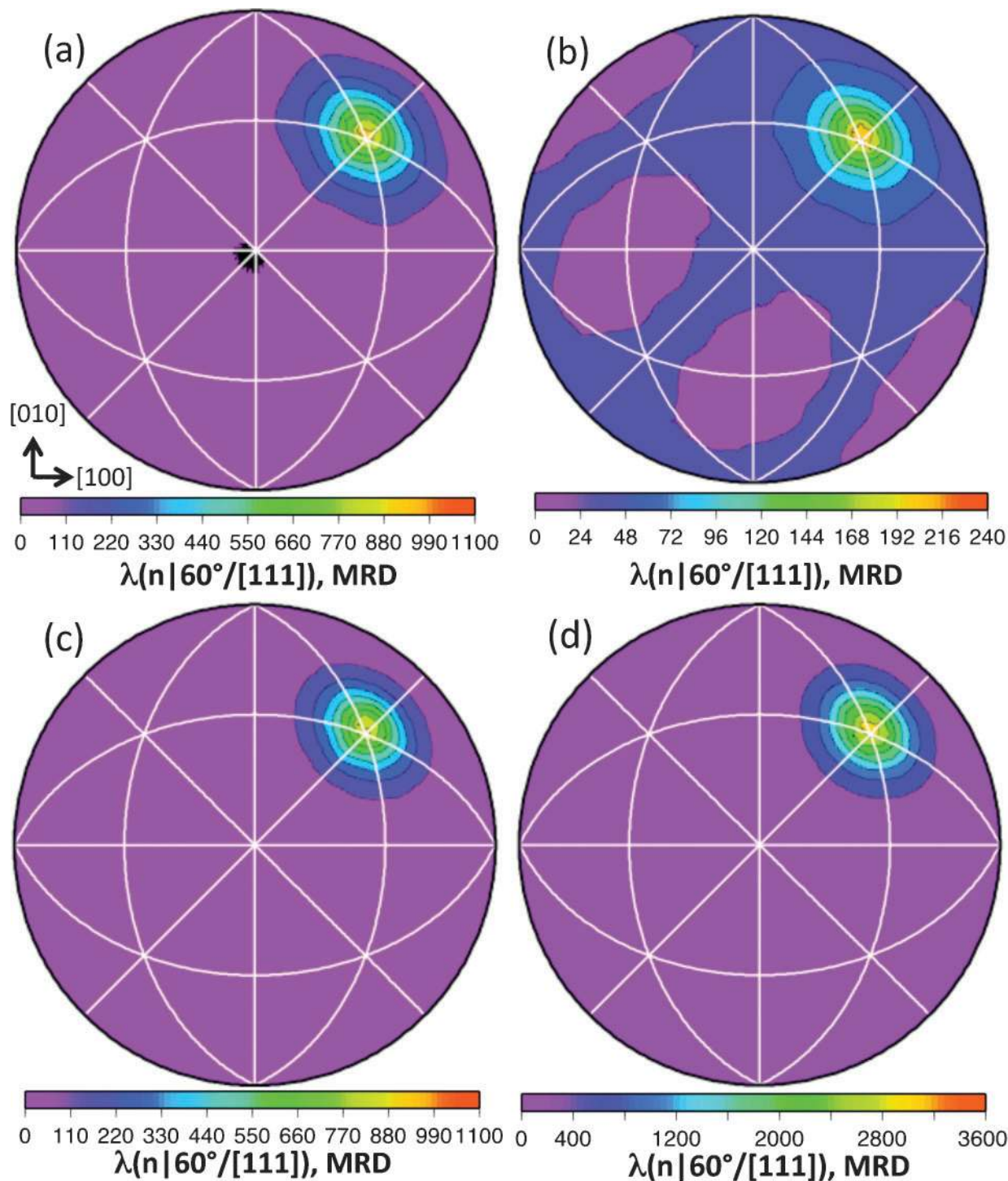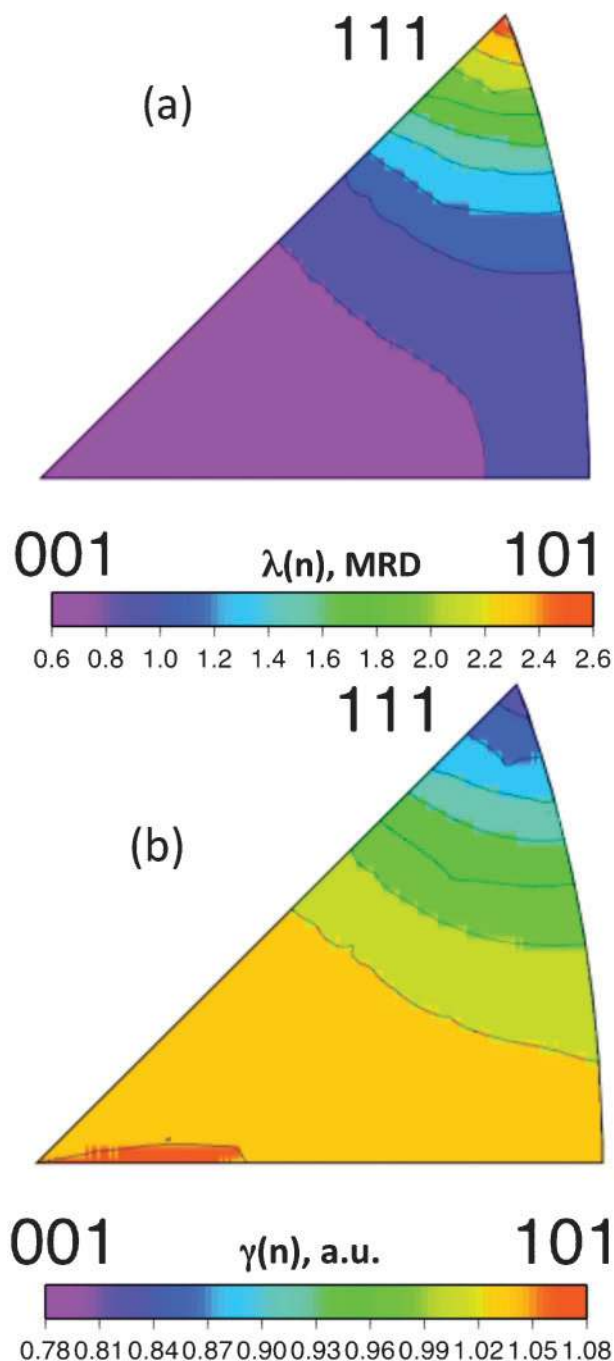
a determined from stereology; b determined from three-dimensional analysis with 1:1 out-of-plane to in-plane spacing ratio and no secondary alignment; c determined from three-dimensional analysis with 2:1 out-of-plane to in-plane spacing ratio and secondary alignment; d determined from three-dimensional analysis with 2:1 out-of-plane to in-plane spacing ratio, secondary alignment and 11 bins per 90°

7 Grain boundary plane distributions in bicrystal reference frame for Σ3 grain boundary (60°/[111]): distributions are plotted on stereographic projections, and units are multiples of a random distribution (MRD)

misorientation are $\phi_1=45°$, $\Phi=70.5°$ and $\phi_2=45$. Because it is $\cos\Phi$ that is discretised, the limits of each bin occur at intervals of 1/9. For the coherent twin, $\cos\Phi=3/9$, and it therefore falls exactly on the border between bins. As a result, the population of the twin is split between multiple bins and always appears lower than expected. A simple way to ameliorate this pr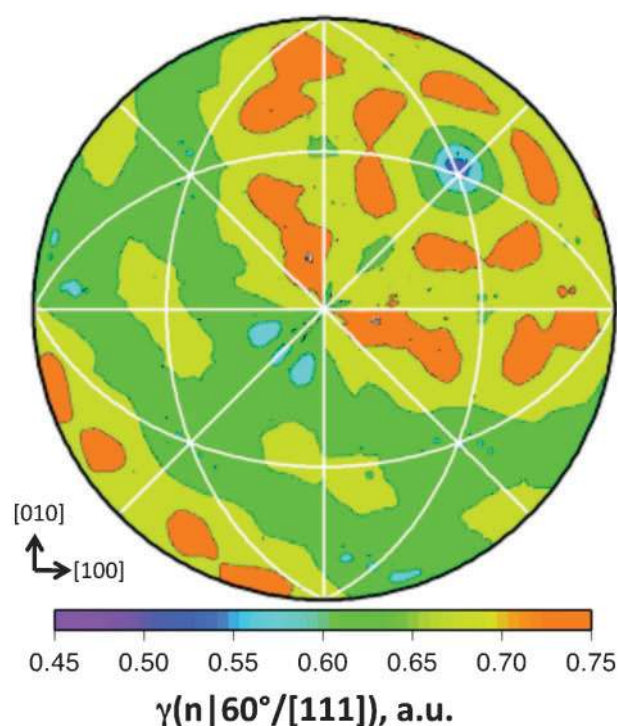oblem is to use a fraction other than 1/9. For example, when the authors used 1/11, the twin population increases to 3600 MRD (Fig. 7d). In this discretisation scheme, there are ~18 000 distinct boundary types, so the authors expect 3900 MRD at the twin orientation. The expectation and observation differ by less than 10%, so the authors conclude that the calculations used to analyse the data and create the distribution are sufficiently accurate.
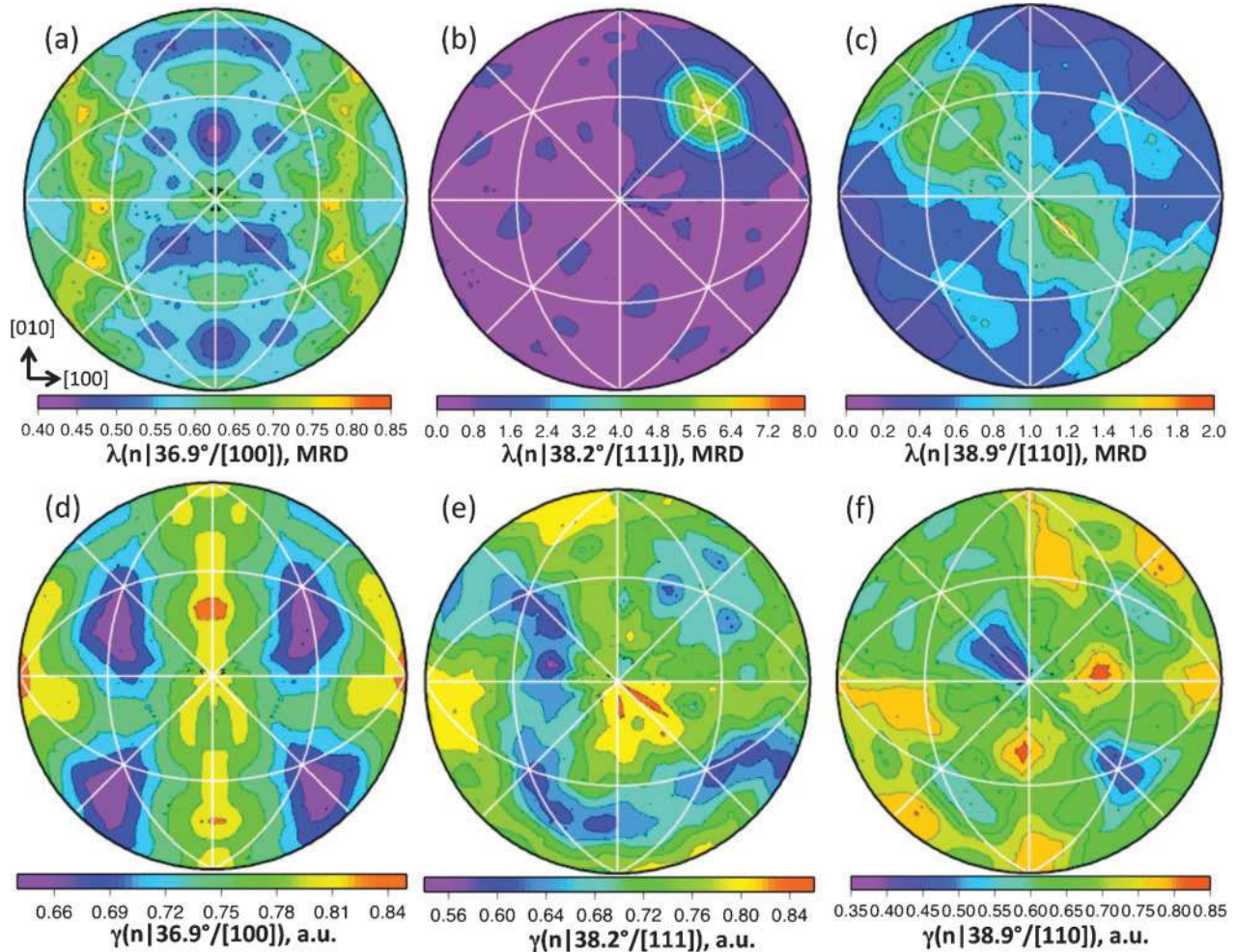
9 Grain boundary energy distribution for grain boundaries with Σ3 misorientation: energies are plotted on stereographic projection, in bicrystal reference frame, and [001] axis is vertical and in centre of plots

8 *a* distribution of grain boundary planes in crystal reference frame, plotted in stereographic projection, and *b* relative grain boundary energies with respect to crystal reference frame

The finer discretisation, however, has the potential to create other artefacts. With 11 bins per 90°, the same amount of data is distributed among almost three times as many bins, so it becomes sparse. Because roughly one-quarter of all boundaries are Σ3 type, this part of the distribution is sufficiently populated at this resolution. However, on average, less than 15% of the boundary types have more than 10 observations. On the other hand, with nine bins per 90°, well over half of the boundary types have more than 10 observations. Therefore, the remainder of the results will be presented from calculations discretised with nine bins per 90°.

The distribution of grain boundary planes in the crystal reference frame is plotted in Fig. 8*a*. This

distribution does not consider the grain boundary misorientation. The minimum of the distribution occurs at [100], and the maximum occurs at [111]. The (111) plane is the closest packed and the habit plane for the twin, so it is presumed to have the lowest energy. This is confirmed by the result in Fig. 8*b*, which shows the relative energy of the grain boundary planes, in the crystal reference frame. The minimum energy occurs at the (111) orientation and the maximum at the (100) position. In other words, when the lattice misorientation is ignored, the grain boundary energy is inversely correlated to the population.

The GBED for the Σ3 grain boundary is shown in Fig. 9. The minimum of the energy occurs at the position of the coherent twin where the population is maximised. As expected, the energy of the twin is the global minimum of the entire GBED (all misorientations), and the relative area of the twin is the global maximum of the GBCD.

The GBCDs and GBEDs for the Σ5, Σ7 and Σ9 misorientations are compared in Fig. 10. The Σ5 grain boundary occurs relatively infrequently; the populations are all less than 1 MRD. The distribution of grain boundary planes for the Σ7 boundary shows a maximum (8 MRD) at the pure twist position, and the grain boundary plane distribution for the Σ9 boundary has a greater than random distribution for tilt grain boundaries (those in the [110] zone). There is a general correspondence between orientations of high population and low energy, and between low population and high energy. However, there are also notable exceptions. For example, the minimum energy configuration of the Σ9 boundary occurs for the asymmetric tilt boundary ($\bar{1}$11)/($1\bar{1}$5), but the maximum population occurs near the position of the ($1\bar{1}$4) symmetric tilt grain boundary.

λ(n|36.9°/[100]), MRD   λ(n|38.2°/[111]), MRD   λ(n|38.9°/[110]), MRD

γ(n|36.9°/[100]), a.u.   γ(n|38.2°/[111]), a.u.   γ(n|38.9°/[110]), a.u.

10 *a–c* **grain boundary plane distributions compared to** *d–f* **grain boundary energy distributions for grain boundaries with** *a*, *c* Σ5, *b*, *d* Σ7 **and** *c*, *f* Σ9 **misorientations: plots are stereographic projections, in bicrystal reference frame, and [001] axis is vertical and in centre of plots**

To illustrate the average relationship between the grain boundary energy and population, the grain boundary energies were categorised into evenly spaced bins of width 0·1 a.u., and the average population and average energy of all of the boundaries in each bin were determined. The logarithms of the average populations are shown in Fig. 11. These data show that, on average, the grain boundary population of a material is inversely correlated to the relative grain boundary energy.

Discussion

The results shown here demonstrate that, to derive accurate grain boundary plane distributions, a secondary alignment procedure that moves the points from a fixed grid is necessary. The majority of the shifts are less than twice the spacing between the orientations (0·25 μm) in the *x* direction. In the *y* direction, it is roughly three times this value. If the uncertainty in the *x* direction is projected onto the sample plane tilted at 70°, it is expanded by a factor of ~3. Therefore, this is thought to be the most likely reason for the difference in the uncertainty in *x* and *y*. However, it is also possible that thermal drift during the measurement or another positioning error during the experiment is responsible for and/or contributes to this effect. Without the

secondary alignment procedure, the observed population is significantly lower than the expected value.

The results also suggest that increasing the out-of-plane to in-plane spacing ratio leads to a more accurate distribution. The spacing between the layers must clearly
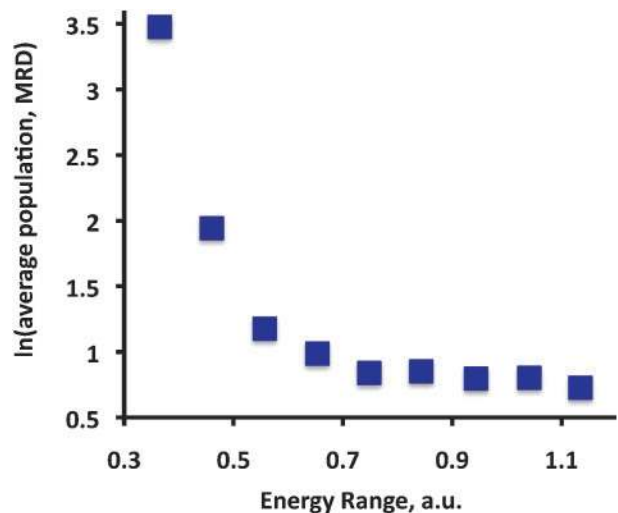
11 Average populations of all grain boundaries with energies that are within range of ±0·05 a.u. of energy on horizontal axis

remain a small fraction of the average grain diameter (ideally, $\leqslant 1/10$), so this means that the spacing between the orientation data in the plane of the EBSD map should be decreased in comparison to the necessary layer spacing.

It is also apparent that the discretisation of the space of grain boundary types influences the results. Those that fall on boundaries between the discrete bins have lower than expected populations, and this happens for the $\Sigma 3$ boundary when there are nine bins per $90°$. When the space is discretised so that there are 11 bins per $90°$, the observed population of $\Sigma 3$ boundaries is only 8% less than the expected value. There are two possible sources for this remaining discrepancy. One is simply that the alignment is imperfect and/or there are other uncorrected distortions. For example, the spacing between layers might not be perfectly uniform or the misalignment may involve a rotation in addition to a translation. A second possibility is that the difference is an artefact of the way the two quantities are calculated. The estimate for the number of twins involves all line segments, while the GBCD calculation involves only those segments that meet at triple junctions. Segments of $\Sigma 3$ boundaries within grains and at the edges of images will not contribute to the GBCD calculation.

The GBCD of this Ni base superalloy has some similarities to the distributions observed in other fcc metals, including aluminum,[7] brass,[9] copper,[12] stainless steel[10] and commercial purity Ni.[12] There are, however, a few distinctions. First, there is a relatively strong peak at the $\Sigma 7$ pure twist boundary formed by two (111) planes. Aluminium is the only one of the previously studied materials that showed a significant population of these boundaries.[7] Another main difference lies in the distribution of grain boundary plane orientations at the $\Sigma 9$ misorientation. The number of $\Sigma 9$ boundaries is relatively low, and the $(1\bar{1}4)$ symmetric boundary is preferred. Once again, this characteristic is similar to aluminum;[7] the other fcc materials prefer asymmetric tilt boundaries.[9,10,12]

Recently, the GBCD and GBED of a 99·999% pure Ni sample have been studied using the same methods.[21] Not surprisingly, many aspects of the distributions are similar. In both cases, the (111) grain boundary planes are the most numerous and have the lowest energy, and (100) planes have the highest energy and are least frequent. Also, the coherent twin is the most frequently occurring boundary and lowest energy boundary. There is also an interesting similarity in the energy anisotropy for the $\Sigma 9$ boundary. In both cases, asymmetric $(\bar{1}11)/(1\bar{1}5)$ tilt boundaries have the minimum energy. While this same asymmetric boundary is the most frequently observed $\Sigma 9$ in pure Ni, IN100 prefers the symmetric $(1\bar{1}4)$ boundary. IN100 also has many fewer $\Sigma 9$ boundaries than the pure Ni.

The difference in the population of $\Sigma 9$ boundaries may stem from the configuration of the $\Sigma 3$ grain boundaries. When two $\Sigma 3$ boundaries that do not share a common misorientation axis meet at a triple junction, the third boundary must be $\Sigma 9$. In the pure Ni sample, 29% of the boundaries (by number) were $\Sigma 3$, and 8·8% were $\Sigma 9$. In IN100, $\Sigma 3$ boundaries make up 14% of the population by number and $\Sigma 9$ make up 2%. This suggests that not as many of the $\Sigma 3$ boundaries in IN100 intersect. A search of the triple junctions indicates that this is true: only 17% of the $\Sigma 9$ boundaries meet at two $\Sigma 3$ boundaries, whereas in the pure Ni, 64% of the $\Sigma 9$ boundaries meet at two $\Sigma 3$ boundaries.

The trend in the data that the grain boundary energy distribution is inversely related to the GBCD is similar to that found previously in other measurements[20,21,28] and in simulations.[32–36] A model has recently been proposed to explain the existence of a steady state GBCD that is inversely related to the grain boundary energy distribution.[37,38] The model is based on the experimental observation that, during grain growth, higher energy boundaries are more likely to be decreasing in area, while lower energy boundaries are more likely to be increasing in area.[38] Based on this, if one assumes that the rate at which grain boundaries are eliminated from the system during critical events is proportional to the grain boundary energy, then steady state distributions with an inverse correlation are produced.[37] However, it should be noted that these conclusions apply only to cases in which the polycrystal is relatively untextured, evolves by normal grain growth, has reached a scale invariant structure and does not have intergranular films or other second phases that affect grain boundary motion. When this is not the case, there are mechanisms that can sustain high mobility grain boundaries, even after they grow past an immediate neighbour and are annihilated.

Conclusion

The distribution of grain boundary planes can be accurately determined from three-dimensional EBSD data. The important factors are the alignment of the parallel layers, the ratio of the out-of-plane to in-plane spacing and the discretisation of the domain of grain boundary types. The grain boundary plane distribution of an IN100 Ni base superalloy shows that, in general, grain boundaries are more likely to be terminated by (111) planes than other orientations. Based on the triple junction geometry, grain boundaries terminated by (111) planes have lower energies than others. On average, the relative areas of different types of grain boundaries are inversely correlated to the relative grain boundary energies.

Acknowledgement

References

1. V. Randle and H. Davies: *Ultramicroscopy*, 2001, **90**, 153–162.
2. D. M. Saylor, A. Morawiec and G. S. Rohrer: *Acta Mater.*, 2003, **51**, 3663–3674.
3. D. M. Saylor, B. S. El-Dasher, T. Sano and G. S. Rohrer: *J. Am. Ceram. Soc.*, 2004, **87**, 670–676.
4. D. J. Rowenhorst and P. W. Voorhees: *Metall. Mater.Trans. A*, 2005, **36A**, 2127–2135.
5. D. J. Rowenhorst, A. Gupta, C. R. Feng and G. Spanos: *Scr. Mater.*, 2006, **55**, 11–16.
6. D. M. Saylor, B. S. El-Dasher, B. L. Adams and G. S. Rohrer: *Metall. Mater. Trans. A*, 2004, **35A**, 1981–1989.
7. D. M. Saylor, B. S. El-Dasher, A. D. Rollett and G. S. Rohrer: *Acta Mater.*, 2004, **52**, 3649–3655.
8. D. M. Saylor, B. S. El-Dasher, Y. Pang, H. M. Miller, P. Wynblatt, A. D. Rollett and G. S. Rohrer: *J. Am. Ceram. Soc.*, 2004, **87**, 724–726.

9. G. S. Rohrer, V. Randle, C.-S. Kim and Y. Hu: *Acta Mater.*, 2006, **54**, 4389–4502.

10. S. T. Downey, II, N. Bembridge, P. N. Kalu, H. M. Miller, G. S. Rohrer and K. Han: *J. Mater. Sci.*, 2007, **42**, 9543–9547.

11. C.-S. Kim, T. R. Massa and G. S. Rohrer: *J. Am. Ceram. Soc.*, 2007, **91**, 996–1001.

12. V. Randle, G. S. Rohrer, H. M. Miller, M. Coleman and G. T. Owen: *Acta Mater.*, 2008, **56**, 2363–2373.

13. V. Randle, G. S. Rohrer and Y. Hu: *Scr. Mater.*, 2008, **58**, 183–186.

14. M. D. Uchic, M. A. Groeber, D. M. Dimiduk and J. P. Simmons: *Scr. Mater.*, 2006, **55**, 23–28.

15. M. A. Groeber, B. K. Haley, M. D. Uchic, D. M. Dimiduk and S. Ghosh: *Mater. Character.*, 2006, **57**, 259–273.

16. J. Konrad, S. Zaefferer and D. Raabe: *Acta Mater.*, 2006, **54**, 1369–1380.

17. A. C. Lewis, K. A. Jordan and A. B. Geltmacher: *Metall. Mater. Trans. A*, 2008, **39A**, 1109–1117.

18. M. Groeber, S. Ghosh, M. D. Uchic and D. M. Dimiduk: *Acta Mater.*, 2008, **56**, 1257–1273.

19. M. Groeber, S. Ghosh, M. D. Uchic and D. M. Dimiduk: *Acta Mater.*, 2008, **56**, 1274–1287.

20. S. J. Dillon and G. S. Rohrer: *J. Am. Ceram. Soc.*, 2009, **92**, 1580–1585.

21. J. Li, S. J. Dillon and G. S. Rohrer: *Acta Mater.*, 2009, **57**, 4304–4311.

22. A. D. Rollett, S.-B. Lee, R. Campman and G. S. Rohrer: *Ann. Rev. Mater. Res.*, 2007, **37**, 627–658.

23. OIMTools: available at: http://mimp.materials.cmu.edu/sftw_data/

24. S. I. Wright and R. J. Larsen: *J. Microsc.*, 2002, **205**, 245–252.

25. G. S. Rohrer, D. M. Saylor, B. S. El-Dasher, B. L. Adams, A. D. Rollett and P. Wynblatt: *Z. Metallkd*, 2004, **95**, 197–214.

26. A. Morawiec: *Acta Mater.*, 2000, **48**, 3525–3532.

27. C. Herring: 'Surface tension as a motivation for sintering,' in 'The physics of powder metallurgy', (ed. W. E. Kingston), 143–179; 1951, New York, McGraw-Hill.

28. D. M. Saylor, A. Morawiec and G. S. Rohrer: *Acta Mater.*, 2003, **51**, 3675–86.

29. D. W. Hoffman and J. W. Cahn: *Surf. Sci.*, 1972, **31**, 368.

30. J. W. Cahn and D. W. Hoffman: *Acta Metall.*, 1974, **22**, 1205.

31. D. G. Brandon: *Acta Metall.*, 1966, **14**, 1479.

32. E. A. Holm, G. N. Hassold and M. A. Miodownik: *Acta Mater.*, 2001, **49**, 2981–2991.

33. M. Upmanyu, G. N. Hassold, A Kazaryan, E. A. Holm, Y. Wang, B. Patton and D. J. Srolovitz: *Interf. Sci.*, 2002, **10**, 201–216.

34. A. Kazaryan, Y. Wang, S. A. Dregia and B. R. Patton: *Acta Mater.*, 2002, **50**, 2491–2502.

35. D. Kinderlehrer, I. Livshits, G. S. Rohrer, S. Ta'asan and P. Yu: *Mater. Sci. Forum*, 2004, **467–470**, 1063–1068.

36. J. Gruber, D. C. George, A. P. Kuprat, G. S. Rohrer and A. D. Rollett: *Scr. Mater.*, 2005, **53**, 351–355.

37. G. S. Rohrer, J. Gruber and A. D. Rollett: *Ceram. Trans.*, 2009, **201**, 343–354.

38. S. J. Dillon and G. S. Rohrer: *Acta Mater.*, 2009, **57**, 1–7.